Int. J. Heat Mass Transfer. Vol. 32, No. 11, pp. 2113–2125, 1989
Printed in Great Britain

0017–9310/89 $3.00+0.00

Turbulent transport phenomena in three-dimensional side-dump ramjet combustors

Y. H. HWANG and Y. H. HUNG†
Department of Power Mechanical Engineering, National Tsing Hua University, Hsinchu, Taiwan 30043, R.O.C.

(*Received* 9 *December* 1988 *and in final form* 20 *March* 1989)

Abstract—Numerical analysis has been performed for exploring transport phenomena of three-dimensional (3-D) turbulent flows with or without chemical reaction in ramjet combustors. The turbulence effects on flow property transport for 2-D and 3-D isothermal flow fields are simulated by two two-equation turbulence and the variant turbulence models (i.e. k–ε and k–kl), and results are then compared with the LDV measured data. It is found that the 3-D results predicted by the k–ε turbulence model are both qualitatively and quantitatively consistent with the experimental data. In addition, the turbulent flow with chemical reaction, assumed to be single-phase, diffusion-controlled combustion with negligible radiation heat transfer, is studied. The theoretical results of this reacting flow such as the velocity, temperature fields and surface stream function will be valuable for the hydraulic and thermal design of 3-D side-dump ramjet combustors.

1. INTRODUCTION

THE INTEGRAL ramjet system to be employed in advanced missiles is characterized by severe volume constraints, so dump combustors are usually chosen for use in volume limited ramjets and ducted rocket missile designs. As we know, the conventional flame holder and combustor liners are not contained in such dump combustors, and the recirculation regions formed by the sudden enlargement of the area between the inlet ducts and the combustion chamber severely affect the flame stabilization. Generally, dump combustors can be grouped into two types—coaxial and side-dump combustors—by the characteristics of the air-breathing systems. In coaxial dump combustors, both air and gaseous fuel are conducted into the combustion chamber through the dome plate, and the flow field is mostly axisymmetric so that the axisymmetric Navier–Stokes equations can be applied to numerically predict the characteristics of such combustors [1, 2]. In side-dump combustors, gaseous fuel from a gas generator is injected through the dome plate and the air stream is supplied through the inlet ducts attached to the combustor periphery. Therefore, the flow field and the fuel–air mixing process in side-dump combustors will be more complicated than that in coaxial dump combustors, in which both air and fuel streams do not bend to a large extent as they flow from the inlet ports to the combustion chamber.

Unlike coaxial dump combustors, there are only a few investigations on side-dump combustors in the existing literature. Shahaf *et al.* [3] analytically and experimentally studied the flow field in a two-dimensional (2-D) side-dump square combustor model of a liquid-fuel ramjet. They simulated the isothermal flow patterns by calculating the distributions of stream function and vorticity, and the turbulent effect was interpreted by a k–kl two-equation turbulence model. Large discrepancies between the measured and calculated axial mean velocity profiles were found along the combustor axis and in the recirculating zones. In 1982, Choudhury [4] tested a side-dump gas generator ramjet with four side inlet ports for the air stream, and concluded that the system of vortices at the head of the combustor is crucial to the stable operation of the flame. However, there is no detailed information about flow structure presented in that paper. Stull *et al.* [5] presented flow visualization photographs of a three-dimensional (3-D) side-dump combustor in a water tunnel, and Vanka *et al.* [6] performed analytical investigations on such a combustor. The calculated results agreed qualitatively with flow visualization photographs; however, a vortex pattern in the dome region shown in their experimental flow visualization could not be predicted in their theoretical calculations. Recently, Liou *et al.* [7, 8] used the axisymmetric Navier–Stokes equations to theoretically predict the flow fields of ramjet combustors with an annular side inlet. They found that the main mechanisms of the strength of recirculating flows in dome regions were composed of both entrainment and impingement effects accompanied with the side-inlet jet flows. Furthermore, Liou and Wu [9, 10] measured the flow field of 3-D isothermal turbulent flow in side-dump combustors by using laser-Doppler velocimetry (LDV). However, no reasonable theoretical analysis for exploring the 3-D flow structure in the combustor is achieved in the existing literature. Hence, the measured results presented in ref. [10] may

† Author to whom correspondence should be addressed.

NOMENCLATURE

C_1, C_2, C_μ constants in k–ε turbulence model
C_{kl}, C_b, C_l, C_s constants in k–kl turbulence model
C_{g1}, C_{g2} constants in combustion model
$C_{p,i}$ specific heat of species i
D_c combustor diameter
f normalized concentration variable, defined in equation (10)
g time-mean square of fluctuation of f
H_{fu} heat of reaction
h stagnation enthalpy
k turbulence kinetic energy
L_d dome height of combustor
l mixing length
M molecular weight of mixture
M_i molecular weight of species i
m_i mass fraction of species i
$\dot{m}_{in}$ inlet flow rate
$\dot{m}_{ri}$ reversal flow rate in dome region
$\dot{m}_{ro}$ forward flow rate in dome region
P pressure
$P(f)$ probability density function of f
R universal gas constant
R_c combustor radial coordinate
R_c^* normalized combustor radial coordinate, $R_c/(D_c/2)$
Re_c combustor Reynolds number, $\rho U_{ref} D_c/\mu_l$
T temperature
U axial mean velocity
U_{ref} combustor bulk mean velocity
V radial mean velocity
$\mathbf{V}$ velocity vector
W azimuthal mean velocity
X_c combustor axial coordinate
X_c^* normalized combustor axial coordinate, $X_c \leqslant 0: X_c^* = X_c/L_d$, $X_c \geqslant 0: X_c^* = X_c/D_c$.

Greek symbols
ε dissipation rate of turbulence kinetic energy
θ_c combustor azimuthal coordinate
μ_l molecular dynamic viscosity
μ_t turbulent dynamic viscosity
ρ fluid density
σ_k, σ_ε, σ_{kl}, σ_f, σ_g turbulent Prandtl number of k, ε, kl, f, and g, respectively
ψ_i concentration variable.

be a good comparison basis for a theoretical study of isothermal flow characteristics in 3-D side-dump combustors.

As for reacting-flow studies, Chen and Tao [11] investigated an axisymmetric reacting fuel-rich side-dump combustor with an annular side inlet port. In 1985, Vanka *et al.* [12] further performed calculations of the 3-D reacting flow field in a side-dump combustor with air injected through two 45° inlet ducts. There were no experimental data and other theoretical results to validate the turbulence and combustion models as well as the grid size in their calculations.

According to the foregoing literature survey, the objectives of the present study are: (1) to perform a 3-D computation of side-dump combustor flow fields without chemical reaction for validating the applicability of the assumed axisymmetric flows in such combustors [7, 8]; (2) to make a comparison between two theoretical results, which are calculated by using two different turbulent models (i.e. k–ε and k–kl); and (3) to present valuable results for turbulent flow and thermal characteristics with chemical reaction in 3-D side-dump combustors.

2. THEORETICAL ANALYSIS

2.1. *Governing equations*

Since the flow recirculation is expected in all space directions for the cases with axisymmetric or with 3-D flow fields, the fully elliptic steady-state Navier–Stokes equations should be numerically solved. Furthermore, in order to make the present turbulent-flow analysis practical, a Reynolds average process is imposed on all instantaneous governing equations. That is, the instantaneous value of any turbulent flow property ϕ is represented by the sum of a time-average component $\bar{\phi}$, and a fluctuating component φ (i.e. $\phi = \bar{\phi} + \varphi$). Therefore, the governing equations can be expressed in the tensor notation as follows.

Continuity

$$\frac{\partial(\rho U_i)}{\partial X_i} = 0. \tag{1}$$

Momentum

$$\frac{\partial}{\partial X_i}(\rho U_i U_j) = -\frac{\partial P}{\partial X_j} + \frac{\partial}{\partial X_i}\left[\mu_l\left(\frac{\partial U_i}{\partial X_j} + \frac{\partial U_j}{\partial X_i}\right) - \rho\overline{u_i u_j}\right]. \tag{2}$$

Note that the body force term has been neglected in the momentum equation. The turbulence correlation $\overline{u_i u_j}$ is the time average of $u_i u_j$ and represents the Reynolds stresses, which have to be modelled to close the above set of equations.

In the present analysis, there are two two-equation turbulence models, i.e. k–ε and k–kl models, adopted

to complete the closure problem of turbulent flow for comparisons. From the generalized Boussinesq eddy viscosity concept, in analogy with the laminar flow, the Reynolds stresses can be expressed as

$$-\rho\overline{u_i u_j} = \mu_t\left(\frac{\partial U_i}{\partial X_j}+\frac{\partial U_j}{\partial X_i}\right)-\frac{2}{3}\delta_{ij}\rho k \tag{3}$$

where δ_{ij} is the Kronecker-delta function and μ_t is the turbulent viscosity that may be related to the relevant variables in different turbulence models.

(i) In the k–ε model

$$\mu_t = C_\mu \rho k^2/\varepsilon. \tag{4}$$

(ii) In the k–kl model

$$\mu_t = C_{kl}\rho k^{1/2} l. \tag{5}$$

The differential governing equation for k can be generalized as

$$\frac{\partial}{\partial X_j}(\rho U_j k) = \frac{\partial}{\partial X_j}\left[(\mu_l+\mu_t/\sigma_k)\frac{\partial k}{\partial X_j}\right] - \rho\overline{u_i u_j}\frac{\partial U_i}{\partial X_j} - C_\mu \rho^2 k^2/\mu_t \tag{6}$$

and the modelled equations for ε and kl are

$$\frac{\partial}{\partial X_j}(\rho U_j \varepsilon) = \frac{\partial}{\partial X_j}\left[(\mu_l+\mu_t/\sigma_\varepsilon)\frac{\partial \varepsilon}{\partial X_j}\right] - C_1\frac{k}{\varepsilon}\rho\overline{u_i u_j}\frac{\partial U_i}{\partial X_j} - C_2\rho\varepsilon^2/k \tag{7}$$

$$\frac{\partial}{\partial X_j}(\rho U_j kl) = \frac{\partial}{\partial X_j}\left[(\mu_l+\mu_t/\sigma_{kl})\frac{\partial kl}{\partial X_j}\right] - C_b l\rho\overline{u_i u_j}\frac{\partial U_i}{\partial X_j} - kl\left[\frac{C_s k^{1/2}\rho}{l}+\frac{\rho C_l(\partial k/\partial X_j)^2}{k^{3/2}}\right]. \tag{8}$$

To show the superiority of the k–ε model over the k–kl model as compared with the experimental results measured in ref. [10], the k–kl turbulence model is adopted as an alternative to the turbulence model in the computation of 3-D isothermal flow.

For isothermal flows, the set of six governing equations mentioned above, containing six unknowns, U, V, W, P, k, and ε (or kl), completes the closure problem of turbulent flows. As for reacting flow, a combustion model has to be proposed to relate the temperature and density variations. In this study, the chemical reaction is assumed to be fast and to occur in one step by the following relation:

$$1\,\text{kg fuel} + i\,\text{kg oxidant} = (1+i)\,\text{kg products}. \tag{9}$$

Therefore, the combustion process is limited by the mixing of the fuel and air streams. The distribution of the mass fraction of fuel and air can be achieved by solving an equation for a conserved scalar, defined as

$$f = \frac{\varphi-\varphi_A}{\varphi_F-\varphi_A} \tag{10}$$

where $\varphi \equiv m_{fu}-m_{ox}/i$ and the subscripts F and A denote the fuel and air stream, respectively. The statistical nature of mixing is interpreted through a two-parameter probability density function, which will be conformed by solving the transport equations of mean (f) and variance (g) of the conserved scalar

$$\frac{\partial}{\partial X_j}(\rho U_j f) = \frac{\partial}{\partial X_j}\left[(\mu_l+\mu_t/\sigma_f)\frac{\partial f}{\partial X_j}\right] \tag{11}$$

$$\frac{\partial}{\partial X_j}(\rho U_j g) = \frac{\partial}{\partial X_j}\left[(\mu_l+\mu_t/\sigma_g)\frac{\partial g}{\partial X_j}\right] + C_{g1}\mu_t\left(\frac{\partial f}{\partial X_j}\right)^2 - C_{g2}\rho\frac{\varepsilon}{k}g. \tag{12}$$

In this work, a battlement shaped probability density function (double delta function) $P(f)$ is assumed and expressed as

$$P(f) = \alpha f_+ + (1-\alpha)f_- \tag{13}$$

where f_+ and f_- are the two extreme values of f, which are given by f and g [13] and expressed as

$$f_+ = \min(f+g^{1/2}, 1.0)$$
$$f_- = \max(f-g^{1/2}, 0). \tag{14}$$

The value of α in equation (13) can be determined from the following relations [14]:

(i) $f_+ < 1.0, f_- > 0 : \alpha = 0.5$
(ii) $f_+ < 1.0, f_- = 0 : \alpha = f^2/(f^2+g)$
(iii) $f_+ = 1.0, f_- > 0 : \alpha = g/[(1-f)^2+g]$
(iv) $f_+ = 1.0, f_- = 0 : \alpha = f$.

All the scalar values expressed in terms of f have been calculated from the determined distribution of $P(f)$ by

$$\bar{\phi} = \int_0^1 P(f)\phi\, df. \tag{15}$$

The density of the mixture of fuel, oxidant and combustion product is represented by the state equation of a perfect gas

$$\rho = \frac{PM}{RT} \tag{16}$$

where R is the universal gas constant and M the mixture molecular weight which is calculated from

$$\frac{1}{M} = \frac{m_{fu}}{M_{fu}}+\frac{m_{ox}}{M_{ox}}+\frac{m_{pr}}{M_{pr}}. \tag{17}$$

The relation of temperature T and f can be derived from

$$h = m_{fu}H_{fu} + C_p T + \tfrac{1}{2}(U^2+V^2+W^2) \tag{18}$$

where h is the stagnation enthalpy, H_{fu} the heat of reaction, and C_p the mixture specific heat which can be

Table 1. Constants in turbulence models

C_b	C_{kl}	C_l	C_h	C_ε	C_μ	C_1	C_2	σ_k	σ_{kl}	σ_ε	σ_f	σ_g
1.0	0.22	1.0	0.416	0.057	0.09	1.44	1.92	1.0	1.2	1.217	0.9	0.9

obtained by the linear combination of the component specific heats as follows:

$$C_p = C_{p,\mathrm{fu}} m_{\mathrm{fu}} + C_{p,\mathrm{ox}} m_{\mathrm{ox}} + C_{p,\mathrm{pr}} m_{\mathrm{pr}}. \quad (19)$$

As mentioned in refs. [12, 15], the adiabatic wall may be considered as an extreme condition of the temperature distribution for the criterion of combustor design. Thus, if the adiabatic wall is assumed in the present study, the stagnation enthalpy related to the local value of f can be expressed as

$$h = f(h_{\mathrm{F}} - h_{\mathrm{A}}) + h_{\mathrm{A}}. \quad (20)$$

Therefore, through the auxiliary equations of the combustion model, the combustion process will interact with fluid dynamic characteristics in the theoretical analysis, and all unknown variables together with governing equations will correctly match to solve turbulent reacting-flow problems with appropriate boundary conditions. Here, it should be mentioned that the rate controlling source terms, for the combustion model employed in the present study, have been eliminated since the Schvab–Zeldovich formulation is adopted (i.e. $\varphi \equiv m_{\mathrm{fu}} - m_{\mathrm{ox}}/i$, $h = m_{\mathrm{fu}} H_{\mathrm{fu}} + C_p T + \frac{1}{2}(U^2 + V^2 + W^2)$) [16, 17].

All modelling constants in turbulence and combustion models are tabulated in Table 1.

2.2. *Boundary conditions*

The set of elliptic partial differential equations mentioned above has to be solved with the following boundary conditions.

(i) Symmetric planes (at $\theta_c = 0^\circ$ and 90°)

$$\frac{\partial U}{\partial \theta_c} = \frac{\partial V}{\partial \theta_c} = \frac{\partial k}{\partial \theta_c} = \frac{\partial \varepsilon}{\partial \theta_c} = 0;\ W = 0$$
$$\frac{\partial f}{\partial \theta_c} = \frac{\partial g}{\partial \theta_c} = 0 \text{ (only for reacting flow).} \quad (21)$$

Note that these boundary conditions will vanish if an axisymmetric assumption is made.

(ii) Combustor axis ($R_c = 0$)

$$\frac{\partial U}{\partial R_c} = \frac{\partial k}{\partial R_c} = \frac{\partial \varepsilon}{\partial R_c} = 0;\ V = W = 0$$
$$\frac{\partial f}{\partial R_c} = \frac{\partial g}{\partial R_c} = 0 \text{ (only for reacting flow).} \quad (22)$$

(iii) Exit

$$\frac{\partial U}{\partial X_c} = \frac{\partial k}{\partial X_c} = \frac{\partial \varepsilon}{\partial X_c} = 0;\ V = W = 0$$
$$\frac{\partial f}{\partial X_c} = \frac{\partial g}{\partial X_c} = 0 \text{ (only for reacting flow).} \quad (23)$$

In this study, the location of the computational downstream boundary is determined by both the measured results [10] and the computational tests. In fact, the computational tests show that there is no noticeable change in the flow field as long as the location of the exit plane is far enough to allow the flow to present one-way dominated behaviour. The outlet flux of conserved scalar f at the exit is also checked with the inlet total flux to ensure the overall consistency in this calculation.

(iv) Inlet. There is no axial inlet on the dome plate in the calculation of isothermal flows. For 3-D isothermal flow which is compared with the measured results [10], the inlet distributions of mean velocities and turbulent kinetic energy at the side-inlet port are introduced directly from the measured results [9]. The distribution of ε is deduced from the assumed uniform turbulence transport length scale $k^{3/2}/\varepsilon$, which is assigned as $0.005(D_c/2)$. On the contrary, the distributions of mean velocities and turbulence kinetic energy at the side-inlet port are set uniform, and the turbulence intensity is assigned as 0.003 in the axisymmetric flow. The magnitude of side-inlet velocity for 2-D axisymmetric cases is maintained at the same bulk mean velocity in the combustor as in the 3-D computations.

As for 3-D reacting flow, the inlet conditions at axial and side inlets as well as thermochemistry properties of fuel and air streams are shown in Table 2. Fuel corresponding to the assigned properties in Table 2 is a solid propellant of 50% polyester and 50% ammonium perchlorate by weight. Although the fuel is a solid propellant, it will be in a gaseous phase as it flows into the combustion chamber. Furthermore, the values of f in air and fuel streams, according to equation (10), are 0 and 1.0, respectively.

(v) Walls

$$U = V = W = 0. \quad (24)$$

In the present study, the flow properties are simu-

Table 2. Inlet conditions of fuel and air stream with their thermochemistry data

Inlet condition or thermochemistry data	Fuel†	Air	Product
Pressure (N m^{-2})	4×10^5	4×10^5	
Temperature (K)	1089	500	
Velocity (m s^{-1})	100	200	
Average specific heat (J kg^{-1} K^{-1})	9381.5	1000	1863.8
Average molecular weight (g mol^{-1})	20.76	28.97	27.87
Heat of combustion (J kg^{-1})	9.8×10^6		

† Fuel: 50% polyester and 50% ammonium perchlorate by weight.

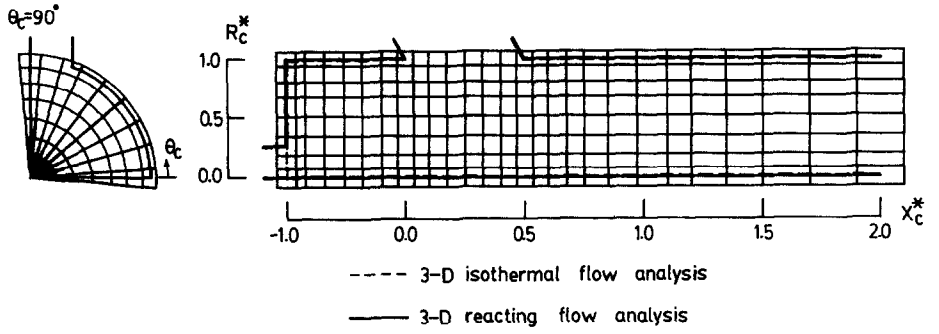

FIG. 1. Grid system employed in the present analysis.

lated by a semi-empirical two-zone algebraic model, i.e. the viscous sublayer and fully turbulent zones, and the so-called wall function [18] is used as a bridge to the viscous layer. For reacting flow, the walls are set adiabatic for heat and mass transports, that is, the heat and mass transfer between the combustor and its surroundings is neglected in this analysis.

2.3. *Numerical method*

The whole set of differential equations for continuity, momentum, turbulence and combustion models with their boundary conditions are first reduced to finite-difference equations by integrating over small discrete control volumes formed in the arranged grid systems. Staggered grid systems are employed. Figure 1 shows the grid arrangement for all scalar variables, such as pressure, density, turbulent kinetic energy, mixture fractions and temperature, etc.; and the velocities are located between two neighbouring scalar variables to represent the true convective quantities across the boundary of such control volumes. The power-law scheme [19] is applied to compromise the convective and diffusive fluxes on the faces of control volumes.

The governing finite-difference equations are then solved by using the line iterative numerical scheme based on the SIMPLE (semi-implicit pressure-link equations) algorithm, which benefits staggered grid systems [20]. Furthermore, in order to prevent numerical instability, the successive changes of the flow variables are underrelaxed with their old values. The new value of a general variable, ϕ, is taken as

$$\phi = \beta\phi^{n} + (1-\beta)\phi^{\circ} \tag{25}$$

where ϕ^{n} is the value computed with no underrelaxation, ϕ° the old iterative value, and β the underrelaxation factor. The underrelaxation factors with their corresponding variables in the present calculations are listed in Table 3. The general structure of the final finite-difference equation for point p is

Table 3. Under-relaxation factors used in the present computations

ϕ	k	kl	P	U	V	W	ε	μ_t
β	0.5	0.5	0.3	0.5	0.5	0.5	0.5	0.5

$$A_{p}\phi_{p} = \sum_{n} A_{n}\phi_{n} + S^{u} + S^{p}\phi_{p} \tag{26}$$

where A_p and A_n are the finite-difference coefficients for point p and its four or six neighbours. S^u and S^p are the integrated source terms, S^p being the linearized part. Equation (26) is solved by repeated alternate line sweeps in all coordinate directions. At each line, a line by line TDMA (tri-diagonal matrix algorithm) is used to solve the linearized system algebraic equations.

For the axisymmetric case, the calculations are made with different grid systems to check the grid independence requirement. The acceptable grid system for 3-D calculations is deduced from the axisymmetric analysis and is shown in Fig. 2. Furthermore, a large number of grid points are placed in the area where steep variations in velocities were revealed from the previous experimental work [10]. Typically, convergence needs 200, 400, 800, and 1500 iterations for axisymmetric, 3-D isothermal k–ε, 3-D k–kl and 3-D reacting flows, respectively; and each iteration needs 3–4 s CPU time on a CDC-CYBER 180/840 computer system in National Tsing Hua University.

3. RESULTS AND DISCUSSION

For selecting a reasonable non-uniform grid system to deal with the 2-D problems, five kinds of grids are chosen for numerical experiments, i.e. 40(axial) × 5(radial), 40×7, 40×9, 40×12 and 40×14. The results show that the relative deviations of the recirculating flow rates along the axial direction in the dome region between 40×9 and 40×14 are less than 2.50%. In addition, the axial mean velocity profiles at $X_c^* = -0.56$ are also checked for various grid arrangements. It is found that the relative deviations between 40×9 and 40×14 are less than 5%. Therefore, the computations are accepted to perform with a 40×9 non-uniform grid system in the 2-D calculations. Furthermore, the corresponding grids are proposed to be used for the 3-D analysis in the X_c and R_c directions.

3.1. *Isothermal flow field in a 2-D side-dump combustor*

Generally, an annular side-dump inlet condition is assumed for analysing a 2-D flow field in side-dump ramjet combustors. According to the geometric sym-

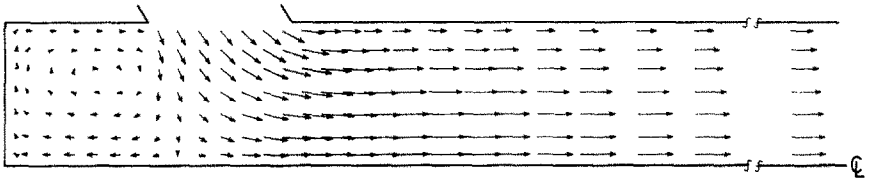

FIG. 2. Vector plot of isothermal flow pattern in 2-D side-dump combustor.

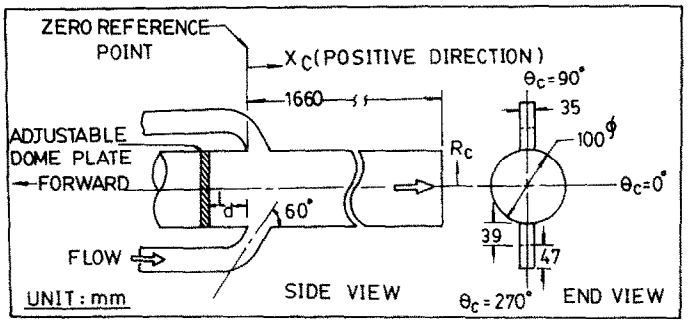

FIG. 3. Schematic of dual-inlet side-dump combustor in 3-D isothermal flow analysis.

metry, the numerical modelling to depict the flow field may be simplified because of no velocity component in the θ_c direction. Figure 2 shows the distribution of the average velocity vector in a 2-D side-dump combustor. In the figure, a closed-type recirculating zone is found between the flow side-dump inlet port and the dome plate, the flow-properties exchange in this recirculating zone is mainly controlled by the inlet air-jet entrainment and flow diffusion. Moreover, there is no secondary recirculating zone near the wall immediately downstream of the dump inlet when the dump angle is less than 75° [5]. Besides, the flow entering the combustion chamber is very fast reaching fully-developed conditions as $X_c^* > 0.75$, i.e. the so-called one-way dominated flow. From the above results, although the 2-D analysis may give a preliminary result which depicts the flow field in the chamber, these calculated results are very difficult to verify by using an experimental technique, which is designed with the basis of 2-D assumptions. Therefore, it is agreed that the development of a generalized 3-D analysis is valuable to verify the feasibility of using 2-D assumptions for the real 3-D complicated configurations.

3.2. *Isothermal flow field in a 3-D side-dump combustor*

As compared with the experimental results presented in ref. [10], the analysis of the 3-D flow fields can be taken to validate a better selection of turbulence models and the feasibility of using 2-D assumptions. There are two different turbulence models adopted in the present research, i.e. the k–ε and k–kl models. The dimensions of the side-dump combustion chamber in the analysis are identical with those of the experimental setup in ref. [10] (see Fig. 3). Owing to large computing resources required, the grid independency study cannot be undertaken for the 3-D cases, so only a $40 \times 9 \times 10$ grid arrangement in the axial, radial, and azimuthal directions is used in the present study. Figure 1 indicates the locations of all scalar variables such as P, k, ε, and T in the calculations. The comparisons of the calculated mean velocity profiles with different turbulent models and the measured data in the side-dump combustor are illustrated in Figs. 4–7. Figures 4 and 5 show the radial and axial mean velocity profiles for $\theta_c = 90°$, respectively; and the axial mean velocity profiles for

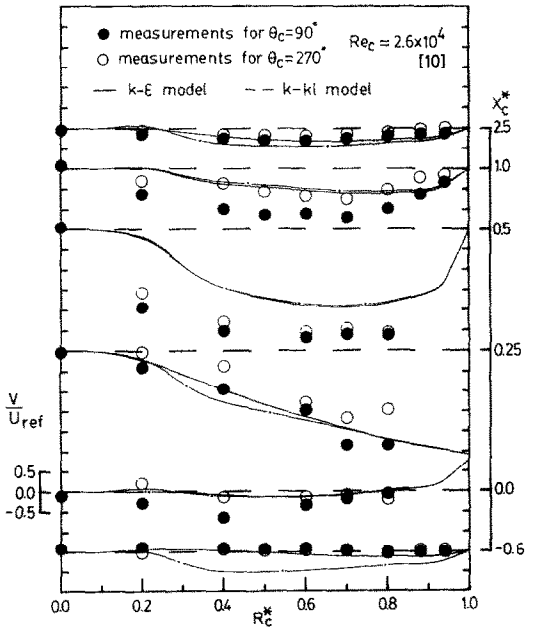

FIG. 4. Radial mean velocity profiles for $\theta_c = 90°$ in 3-D side-dump combustor.

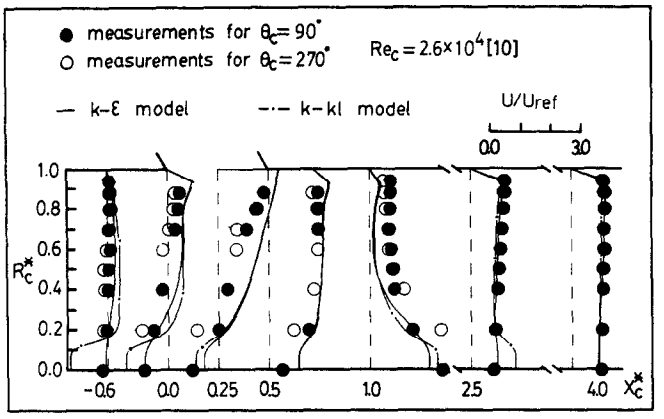

FIG. 5. Axial mean velocity profiles for $\theta_c = 90°$ in 3-D side-dump combustor.

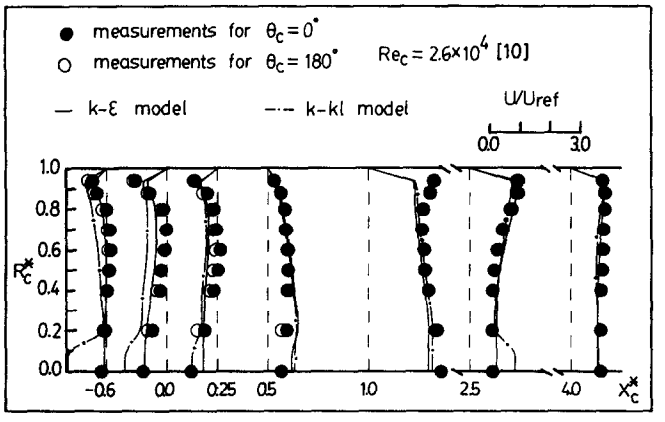

FIG. 6. Axial mean velocity profiles for $\theta_c = 0°$ in 3-D side-dump combustor.

$\theta_c = 0°$ are shown in Fig. 6. Since the computations are adopted with the assumption of symmetry about the combustor axis, the measured data for $\theta_c = 270°$ and 180° [10] are also plotted together with the data for $\theta_c = 90°$ and 0° in the figures. The differences between the mean velocity calculated with two turbulence models in the inlet region (i.e. $0.25 \leqslant X_c^* \leqslant 1.0$) are not significant; while the results evaluated by using the *k–kl* model show a much higher radial mean velocity component in the dome region (i.e. $X_c^* \leqslant 0$), and a much higher axial velocity component near the combustor axis, as compared with those calculated by using the *k–ε* model and the experimental data [10]. Therefore, here it may be concluded that the results calculated with different turbulence models show a significant difference in a certain region, in which the recirculating flows exist and diffusion dominates the flow mechanism. Furthermore, as presented in Figs. 4–6, the calculated results with the *k–ε* model are both in qualitative and quantitative agreement with the experimental data [10]. The deviations between the predicted results with the *k–ε* model and the measured data become insignificant in the dome region and in the far downstream region (i.e. $X_c^* < 0$ and $X_c^* > 1$). In the region of $0 \leqslant X_c^* \leqslant 1.0$ as compared with the experimental data, the calculated results at $\theta_c = 90°$ reveal a weaker radial velocity shown in Fig. 4, and a weaker axial velocity near the combustor axis (i.e. at $\theta_c = 0°$) in Fig. 6. The main reason to bring about these deviations is that the actual inlet conditions in ref. [10] are

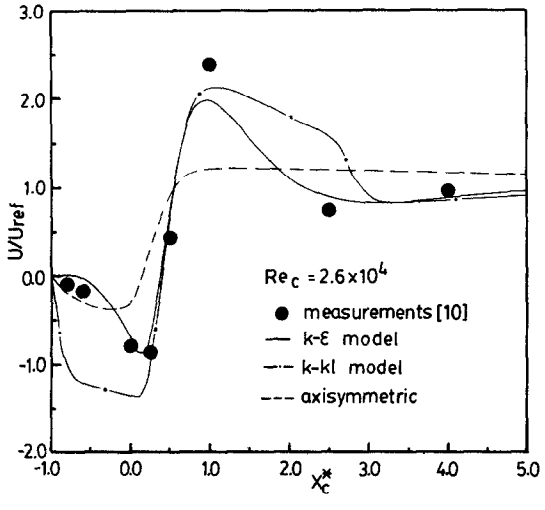

FIG. 7. Distribution of central axial mean velocity in 3-D side-dump combustor.

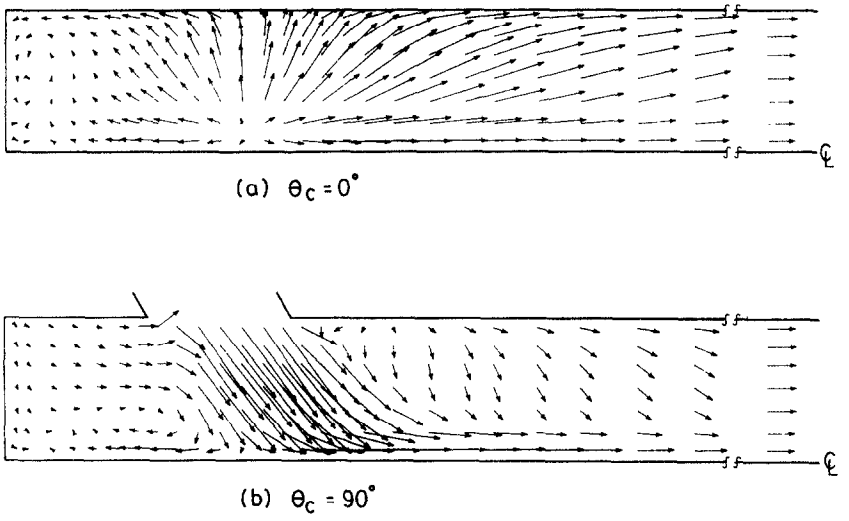

FIG. 8. Vector plots of isothermal flow field in planes of $\theta_c = 0°$ and 90°.

measured at the plane 20 mm above the side-inlet plane ($R_c^* = 1$); while the inlet conditions are exactly set at the side-inlet plane ($R_c^* = 1$) in the present computations. Moreover, the measured velocity component at the inlet plane only prevails in two directions (i.e. $\theta_c = 0°$ and 90°), and the symmetrical flow condition about the combustor axis may not be exactly achieved by controlling the operating condition at the two inlet square ducts in the experiments.

In addition, the distribution of axial mean velocity at the combustor axis, where both the radial and azimuthal velocities vanish, is a good intrusive parameter. The calculated and measured distributions of central mean velocity along the axial direction are presented in Fig. 7. Comparisons between the calculations by using the k–ε and k–kl models are also made in the figure. It is obviously found that the results calculated by using the k–ε model are superior to those using the k–kl model, as compared with the experimental data [10]. In the figure, it is also revealed that there is a larger deviation between the calculated and measured data at $X_c^* = 1.0$. This may be due to the fact that the measured mean velocity reveals highly asymmetric profiles in the region of $0.25 \leqslant X_c^* \leqslant 1.5$, but a symmetric flow pattern is assumed in the present calculation.

Figures 8(a) and (b) show the flow pattern in planes of constant azimuthal angles, $\theta_c = 0°$ and 90°, respectively. In the present calculation, it is found that the vortex motions in different θ_c planes are quite different in the dome region due to the 3-D effects. The recirculating flow in the $\theta_c = 90°$ plane (see Fig. 8(b)), where it rotates clockwise, is driven by the bifurcating flow of jet impingement in the upstream direction and by the shear of the inlet flows. In the $\theta_c = 0°$ plane (see Fig. 8(a)), the recirculating flow is formed by the spread-out effect of the combustor wall both in the radial and upstream directions, and rotates in the counter-clockwise direction. The recirculating flows in the 3-D combustor do not form a closed-loop the same as in the 2-D configuration. They flow into and out of the dome region in a spiral way due to the existence of the azimuthal velocity component. Since the swirling motion is sustained by the inlet jet flows, the azimuthal velocity is more pronounced in the inlet region and decays in other regions of the chamber. Here, a quantitatively defined parameter, swirl intensity (SI), will be chosen to express the evolution of swirling motion more clearly. The expression of SI is

$$SI(X_c^*) = \frac{\int_{A(X_c^*)} \frac{1}{2}\rho W^2 \mathbf{V} \cdot d\mathbf{A}}{-\int_{A_{in}} \frac{1}{2}\rho(U^2 + V^2 + W^2)\mathbf{V} \cdot d\mathbf{A}} \quad (27)$$

where SI denotes the dimensionless axial flux of the swirling mean kinetic energy at a given X_c^*, normalized by the inlet flux of the total mean kinetic energy. It is an index of swirling-motion evolution. Figure 9 shows the distributions of swirling intensity calculated with

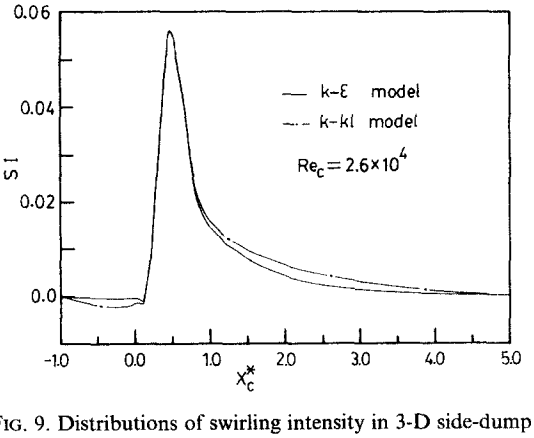

FIG. 9. Distributions of swirling intensity in 3-D side-dump combustor.

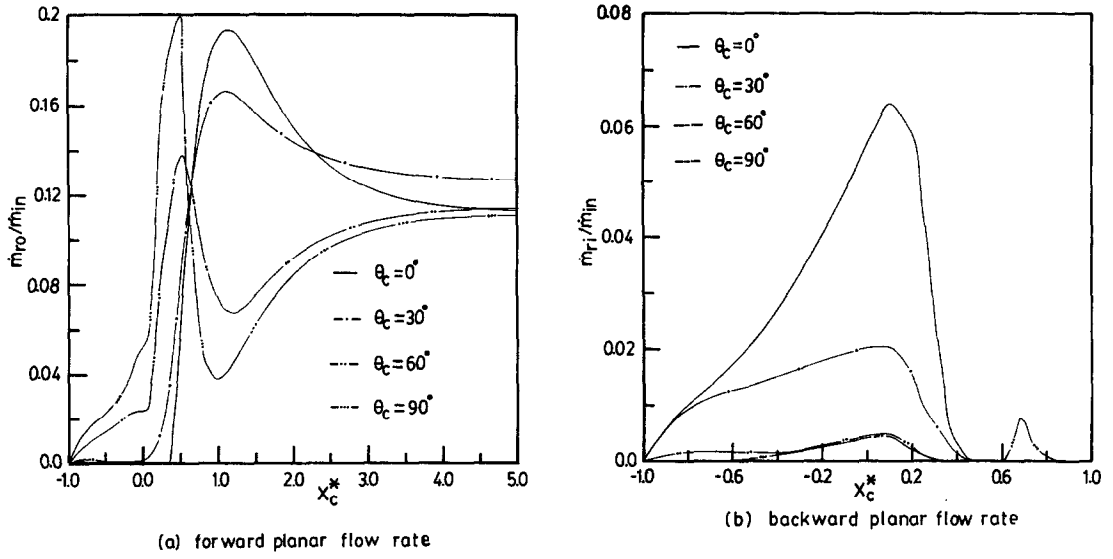

FIG. 10. Dimensionless forward and backward planar flow rate in 3-D side-dump combustor.

the k–ε and k–kl models. The differences between calculations for the *SI* distributions with these two turbulence models are not significant. As for the *SI* distributions at various X_c^* locations in the combustor, it manifests that the vortices are generated due to the impingement of the inlet jets, and the resulting swirl intensity is confined within the range of $0 \leqslant X_c^* \leqslant 2$ with a peak value of 5.6% at $X_c^* = 0.5$. Note that the swirl intensity decays rapidly when $X_c^* > 0.5$, it indicates that a strong turbulent mixing does exist in the region of $X_c^* \leqslant 0.5$. The swirling motion diminishes in the region of $X_c^* > 4.0$; it means that a unidirectional flow has been developed in that region.

As we know, the existence of azimuthal velocity causes the spiral flow structure, and the planar flow rate will be varied at different axial locations. Figures 10(a) and (b) present the forward and backward planar flow rates in the combustor, normalized by the inlet flow rate, respectively. As shown in Fig. 10(a), since the inlet port is located in the range of $62° < \theta_c \leqslant 90°$, the forward flow rate near the plane of $\theta_c = 90°$ is kept at a peak value of about 20% of the inlet flow rate. The swirl motion drives this forward flow from the plane of $\theta_c = 90°$ to that of $\theta_c = 0°$ as $X_c^* > 0.5$. Further downstream, the distinction of velocity profiles in different planes becomes insignificant, and the amount of forward flow rate approaches an asymptotic quantity during the development of unidirectional flow. In the dome region, the swirling motion is not significant, and the entrainment effect of the inlet jet drives the fluid out of this region near the plane of $\theta_c = 90°$. Figure 10(b) shows the distribution of the reversal flow rate toward the dome plate at some specific planes in the dome region. The impingement of inlet jets makes the bifurcating flow, driving the inlet flow into the dome region near the plane of $\theta_c = 0°$. The amount of reversal flow rate decreases to zero from the inlet ($X_c^* = 0$) to the dome plate ($X_c^* = -1.0$), as shown in Fig. 10(b). The reversal flow at $\theta_c = 90°$, occurring immediately downstream of the inlet port ($X_c^* > 0.5$), is brought about by the entrainment effect of the inlet jet, and a secondary recirculating zone similar to that in the 2-D flow field [5] is then evolved. The distribution of planar flow rates will be more comprehensive as it conforms with the flow pattern shown in Figs. 8(a) and (b).

3.3. *Reacting flow field in a 3-D side-dump combustor*

From the above results and discussion, the k–ε turbulence model is capable of predicting the complicated isothermal flow field in side-dump combustors. Therefore, the 3-D isothermal analysis may be extended to explore the reacting flow field of 3-D side-dump combustors with the gaseous fuel conducted through the dome plate. Figures 11(a) and (b) show the flow pattern in the planes of $\theta_c = 0°$ and 90°, respectively. As compared with Fig. 8, the flow pattern in the dome region is significantly influenced by the axial fuel jet flow, which is conducted through the dome plate. The fuel flow enhances the strength of counter-clockwise vortices. As shown in Fig. 11(b), the clockwise vortex is confined within the region near the combustor axis and the inlet region at $\theta_c = 90°$. The counter-clockwise vortex structure at $\theta_c = 0°$ shown in Fig. 11(a) is more intact than that in Fig. 8(a) for an isothermal pure side-dump flow field.

Figures 12(a) and (b) show the isotherm contours along the axial direction at $\theta_c = 0°$ and 90°, respectively. Since the combustion process is assumed to be simply diffusion controlled, and the overall fuel–air ratio is fuel lean, the high temperature region is confined within the dome region and between the axial fuel and side-inlet air flows. That is, the location of the flame originates from the edge of the axial fuel jet flow and is confined in the dome region by the side-inlet air stream. In the dome region, the temperature

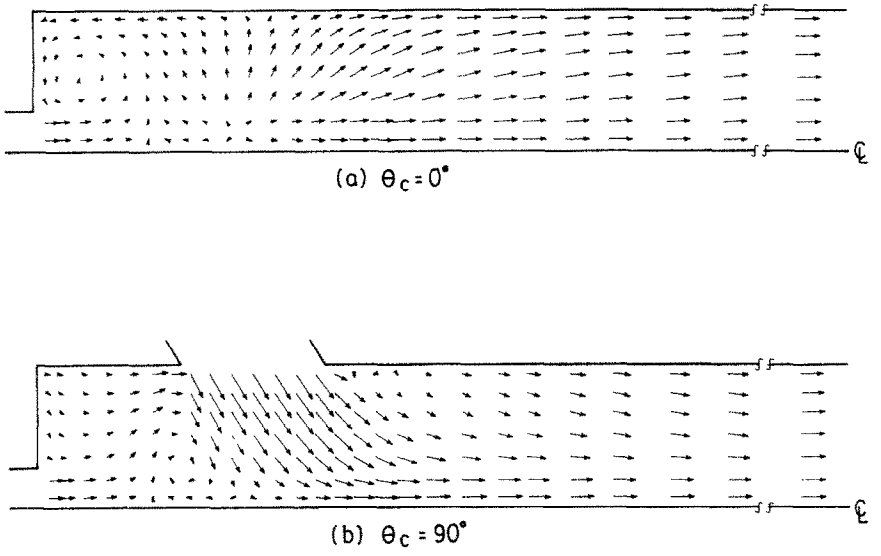

FIG. 11. Vector plots of reacting flow field in 3-D side-dump combustor.

field shows a rather steep gradient and the highest temperature occurs near the combustor side wall. This phenomenon implies that the mixing process is more dominated by the flow structure than by the temperature field accompanied by combustion. In the downstream region, both velocity and concentration mixing are rather complete, and the temperature becomes a uniform distribution between 900 and 1000 K.

Finally, a concept of surface stream lines, which are conventionally employed to describe 3-D external flow separation, may be introduced to depict the complex flow patterns in the present study. As we know, the surface stream lines for steady flow are tangential at every point to the surface flow direction. On the surface, velocity is zero, but there exist stream lines which pass through points at a distance h measured from the wall surface; therefore, surface stream lines are defined as the flow directions of particles infinitesimally close to the wall [21]. Then surface stream lines are given by

$$\frac{\mathrm{d}(D_c\theta_c/2)}{\mathrm{d}X_c} = \lim_{h\to 0}\frac{W}{U} = \left(\frac{\partial W/\partial R_c}{\partial U/\partial R_c}\right)_{h\to 0}. \tag{28}$$

Generally, there are two types of separation, namely

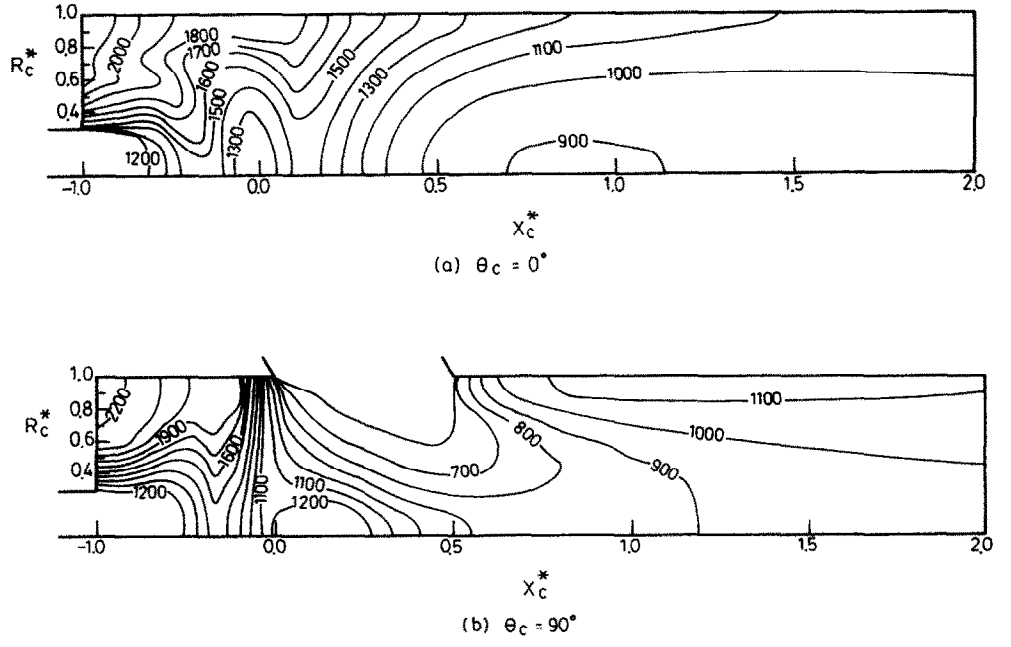

FIG. 12. Isotherm contours of reacting fluid in 3-D side-dump combustor.

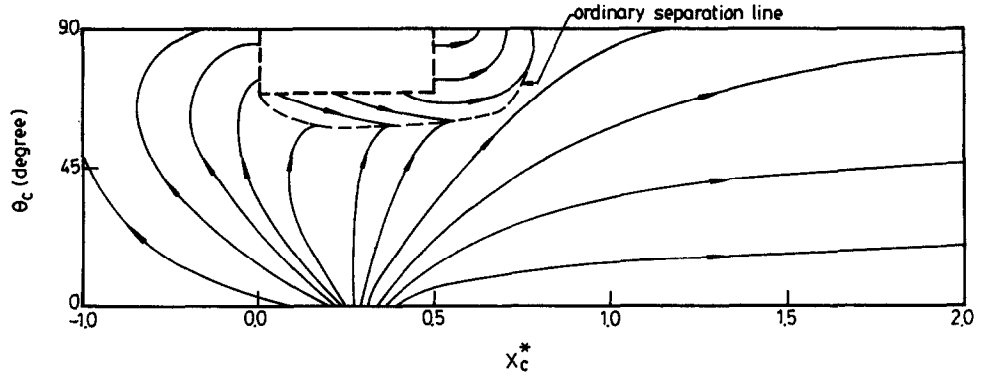

FIG. 13. Surface stream lines of 3-D side-dump combustor.

ordinary and singular. Ordinary separation is common in 3-D flows. Ordinary separation occurs only when two distinct surface stream lines, lying in the solid surface, converge and meet at a point, say, the separation point. They then combine and leave the surface in the form of a single separation stream line. At the separation point where two surface stream lines meet, the slopes of both stream lines are the same. This implies that both surface stream lines must be tangential to each other in the plane or the wall, forming a cusp at the separation point [21]. For the singular separation, the surface stream lines can meet in other than a cusp at a singular point. The only requirement on the singular surface stream lines is that the shear stress must be zero at the wall. It may be recalled in ref. [21], perhaps lines of singular separation never occur in 3-D flows because of the absence of wall shear stress at the separation line, and no one has observed lines of singular separation in 3-D flows.

In the present study, the surface stream lines and wall temperature distributions are shown in Figs. 13 and 14, respectively. From Fig. 13, an ordinary separation line is found in the side-dump inlet region. The occurrence of this 3-D flow separation is due to both effects, that is, the entrance effect of low-temperature side-inlet air flow and the jet-impingement effect of high-temperature reacting flow. Therefore, as compared with the upstream region of the side-inlet air port (i.e. $X_c^* < 0$), a lower temperature distribution can be found in the side-inlet region (see Fig. 14). As shown in Fig. 14, most of the upstream reacting flows, which are almost confined in the dome region, may cause a higher temperature distribution of the combustor surface in that region. Moreover, as shown in Fig. 13, it is also found that the swirling-flow effect gradually diminishes along the axial direction. In the far downstream region, the reacting flows which are fully mixed become unidirectional, and the distribution of wall temperatures then gradually becomes uniform as shown in Fig. 14.

4. CONCLUDING REMARKS

In the present study, the theoretical analysis has been made to investigate the 2-D and 3-D turbulent transport phenomena of isothermal and reacting flows in side-dump ramjet combustors. Meanwhile, there are two distinct turbulence models adopted to complete the closure problem in turbulent flow and compared with the measurement results. From the computational results, it manifests that the simplified 2-D flow field is not adequate to represent the flow characteristics of the real 3-D cases. In the dome region, the structure of the recirculating flow of the 2-D flow field is a closed type and there is no convective interaction between the recirculating flow and the side-inlet jet flow. However, for the 3-D flow field, the

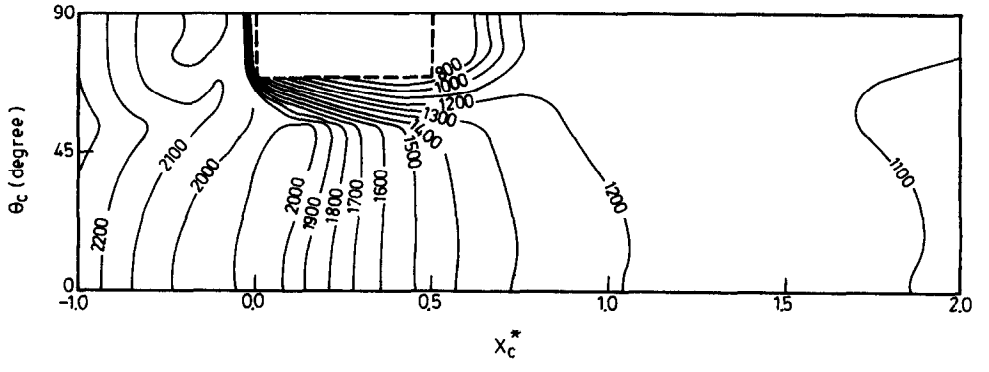

FIG. 14. Isotherm contours on 3-D combustor wall.

recirculating flow in the dome region is an open type and it is the bifurcating flow of the side-inlet jet flow, that is, a part of inlet flow flows into and out of the dome region and forms the so-called recirculating structure. Furthermore, the swirling effect in the 3-D flow induces a helical flow path in the combustor and the flow rates on different θ_c planes are not the same. These phenomena of swirling flow were not observed in the 2-D flow field. It should also be noted that the swirling-flow effect in the 3-D flow is significant in the inlet region and decays rapidly toward the dome region and the downstream region.

The effects of two different turbulence models on the isothermal flow field are also considered in this work. Although in the inlet region, the differences between the results of these two turbulence models are not significant because of the strong convective effect of the side-inlet jet flow, the k–kl turbulence model is not suitable for such a complicated flow field in the side-dump combustors. The results of the k–kl turbulence model give the too high radial mean velocities in the dome region and unusual high axial mean velocities near the combustor axis as compared with the measured results. On the contrary, the flow field calculated with the k–ε turbulence model gives the qualitative and quantitative agreement with experimental results.

Finally, the k–ε turbulence model is chosen to predict the 3-D, turbulent, reacting flow. As compared with the results for the pure side-dump combustor, the flow field in the dome region is significantly influenced by the axial fuel jet flow, which is conducted through the dome plate. Since fuel-lean diffusion-controlled combustion is assumed, the location of the flame is originated from the edge of the axial fuel-jet flow and confined in the dome region by the side-inlet air stream. The wall temperature in the dome region is quite high and the cooling process in this region should be considered to prevent cracking of the combustor material.

REFERENCES

1. J. E. Drewery, Fluid dynamic characterization of sudden-expansion ramjet combustor flowfields, *AIAA J.* **16,** 313–319 (1978).
2. F. H. Tsau and W. C. Strahle, Prediction of turbulent combustion flow fields behind a backward facing step, AIAA-88-0340, AIAA 26th Aerospace Science Meeting, 11–14 January (1988).
3. M. Shahaf, Y. Goldman and J. B. Greenberg, An investigation of impinging jets in flow with sudden expansion, *Proc. 22nd Israel Annual Conf. on Aviation and Astronautics*, pp. 100–106 (1980).
4. P. R. Choudhury, Characteristics of a side dump gas generator ramjet, AIAA-82-1258, AIAA/SAE/ASME 18th Joint Propulsion Conf., Cleveland, Ohio, June (1982).
5. F. D. Stull, R. R. Craig, G. D. Wtreby and S. P. Vanka, Investigation of a dual inlet side dump combustor using liquid injection, *AIAA J. Propul. Pwr* **1,** 83–88 (1985).
6. S. P. Vanka, F. D. Stull and R. R. Craig, Analytical flow fields in side inlet dump combustors, AIAA-83-1399, AIAA/SAE/ASME 19th Joint Propulsion Conf., 27–29 June (1983).
7. T. M. Liou, Y. H. Hung and Y. H. Hwang, A study of flowfields in a side-dump combustor with various dump angles, *J. Chin. Soc. Mech. Engrs* **7,** 253–258 (1986).
8. T. M. Liou, Y. H. Hung and Y. H. Hwang, The effects of dump positions on flowfield in a side-dump combustor, *Trans. Aeronaut. Astronaut. Soc., Taiwan* **18,** 33–39 (1985).
9. T. M. Liou and S. M. Wu, Application of laser velocimetry to the curved inlet duct of a side dump combustor, 3rd Int. Symp. on Applications of Laser-Doppler Anemometry to Fluid Mechanics, Lisbon, Portugal, July (1986).
10. T. M. Liou and S. M. Wu, Flow field in a dual-inlet side-dump combustor, *AIAA J. Propul. Pwr* **4,** 53–60 (1988).
11. L. Chen and C. C. Tao, Study of side-inlet dump combustor of solid ducted rocket with reacting flow, AIAA-84-1378, AIAA/SAE/ASME 20th Joint Propulsion Conf. (1984).
12. S. P. Vanka, R. R. Craig and F. D. Stull, Mixing, chemical reaction and flow development in ducted rockets, AIAA-85-1271, AIAA/SAE/ASME/ASEE 21st Joint Propulsion Conf., Monterey, California (1985).
13. M. A. Serg-El-Din and D. B. Spalding, Computations of three-dimensional gas turbine combustion chamber flows, *Trans. ASME J. Heat Transfer* **101,** 326–336 (1979).
14. E. E. Khalil, *Modelling of Furnaces and Combustors*, pp. 66–68. Academic Press, New York (1982).
15. M. A. Serg-El-Din, The numerical prediction of the flow and combustion processes in a three-dimensional can combustor, Ph.D. thesis, Imperial College of Science and Technology, London (1977).
16. I. Glassman, *Combustion*, pp. 66–67. Academic Press, New York (1977).
17. F. A. Williams, *Combustion Theory* (2nd Edn), pp. 73–76. Addison-Wesley, Reading, Massachusetts (1985).
18. B. E. Launder and D. B. Spalding, The numerical computation of turbulent flows, *Comput. Meth. Appl. Mech. Engng* **3,** 269–289 (1974).
19. S. V. Patankar, *Numerical Heat Transfer and Fluid Flow*, Hemisphere, New York (1980).
20. S. V. Patankar and D. B. Spalding, Calculation procedure in three-dimensional parabolic flows, *Int. J. Heat Mass Transfer* **15,** 1787–1806 (1972).
21. P. K. Chang, *Separation of Flow*, pp. 27–35. Pergamon Press, New York (1970).

PHENOMENE DE TRANSPORT TURBULENT TRIDIMENSIONNEL DANS LES CHAMBRES DE COMBUSTION DE STATO-REACTEURS

Résumé—On développe une analyse numérique pour explorer les phénomènes de transport des écoulements tridimensionnels avec ou sans réaction chimique, dans des chambres de combustion de stato-réacteur. Les effets de la turbulence sur les propriétés de transport des champs d'écoulement isotherme en 2-D et 3-D sont simulés par deux modèles à deux équations de turbulence et de turbulence variante (k–ε et k–kl), et les résultats sont comparés avec les valeurs mesurées. On trouve que les résultats en 3-D obtenus par le modèle k–ε sont qualitativement et quantitativement cohérents avec les données expérimentales. De plus, on étudie l'écoulement turbulent avec reaction chimique, supposé être monophasique, à combustion contrôlée par la diffusion avec un rayonnement thermique négligeable. Les résultats théoriques de cet écoulement réactif concernant les champs de vitesse et de température, les fonctions de courant de surface, sont valables pour le dessin hydraulique et thermique des chambres de combustion de stato-réacteurs.

TURBULENTE DREIDIMENSIONALE TRANSPORTPHÄNOMENE IN EINEM STAUSTRAHLTRIEBWERK MIT SEITLICHEM AUSTRITT

Zusammenfassung—Die dreidimensionale turbulente Strömung mit oder ohne chemische Reaktion in einem Staustrahltriebwerk wird numerisch untersucht. Simuliert wird der Einfluß der Turbulenz auf das Transportverhalten für zwei- und dreidimensionale isotherme Strömungsfelder (k–ε) und (k–kl). Die Ergebnisse werden mit den Messungen eines Laser-Doppler-Anemometers verglichen. Dabei stellt sich heraus, daß die 3-D-Ergebnisse, die sich mit dem k–ε-Turbulenzmodell ergeben, quantitativ und qualitativ mit den experimentellen Daten übereinstimmen. Zusätzlich wird eine turbulente Strömung mit chemischer Reaktion untersucht. Die Strömung wird dabei als einphasig, mit einer durch die Diffusion bestimmten Verbrennung und mit vernachlässigbaren Strahlungsverlusten angenommen. Die theoretischen Ergebnisse dieser Strömung mit Reaktion—wie die Geschwindigkeit, das Temperaturfeld und die Funktion der Grenzflächenströmung—werden für die hydraulische und thermische Auslegung von Staustrahltriebwerken mit seitlichem Austritt sehr nützlich sein.

ТУРБУЛЕНТНЫЕ ЯВЛЕНИЯ ПЕРЕНОСА В ТРЕХМЕРНОЙ НАКЛОННОЙ КАМЕРЕ СГОРАНИЯ ПРЯМОТОЧНОГО ВОЗДУШНО-РЕАКТИВНОГО ДВИГАТЕЛЯ

Аннотация—Выполнен численный анализ явлений переноса при трехмерном турбулентном течении с химической реакцией и без нее в камере сгорания прямоточного воздушно-реактивного двигателя. С помощью двух моделей турбулентности (k–ε и k–kl) смоделировано влияние турбулентности на характеристики переноса для полей двух- и трехмерных изотермических потоков, а затем проведено сранение с измеренными значениями. Найдено, что результаты для трехмерного потока, рассчитанные по модели k–ε, согласуются как качественно, так и количественно с экспериментальными данными. Кроме того, исследовано турбулентное течение с химической реакцией, представленное однофазным потоком с спределяемым диффузией горением и пренебрежимо малым лучистым теплопереносом. Полученные теоретические результаты для полей скорости и температуры, а также для поверхнохтной функции тока можно использовать для гидравлического и теплового расчета трехмерных наклонных камер сгорания прямоточных воздушно-реактивных двигателей.